Visco-plastic self-consistent modeling of crystallographic texture evolution related to slip systems activated during machining Ti-6AL-4V

Qingqing Wang^a, Ravi M. Shankar^{b,*1}, Zhanqiang Liu^{c,*2}

(a School of Mechatronic Engineering, China University of Mining and Technology, Xuzhou 221116, PR China)

b Department of Industrial Engineering, University of Pittsburgh, Pittsburgh, Pennsylvania
15261, USA

c School of Mechanical Engineering, Shandong University, Jinan 250061, PR China

*¹Corresponding author, E-mail address: ravishm@pitt.edu (M.R. Shankar)

*²Corresponding author, E-mail address: melius@sdu.edu.cn

Abstract

Exploring the interconnection between texture variation and the activations of slip systems is vital for the texture generation and controlling during machining of Ti-6AL-4V. The evolution of crystallographic texture and the activations of different slip systems during machining of Ti-6AL-4V were studied combined with the orientation imaging microscopy (OIM) and visco-plastic self-consistent (VPSC) framework. A VPSC model considering the activations of five slip families as well as twinning of hexagonal close packed (HCP) Ti structure and coupled with a finite element cutting simulation model were used to simulate the texture variations during machining of Ti-6AL-4V. Crystallographic texture evolutions of Ti-6AL-4V in chips and machined surface were examined using OIM. Two initial textures of Ti-6AL-4V yielded the same end texture, a strong C fiber texture. Lastly, Voce hardening parameters were modified to control the activations of slip modes as well as twinning and

calibrate the VPSC simulation results of texture and mechanical property. It is found that the combination of prismatic <a>, basal <a>, pyramidal <a> and 2-nd order pyramidal <c+a> slip systems induce the generation of C shear texture in the machining of Ti-6AL-4V. The activation of the 2-nd order <c+a> slip system makes large contribution to the formation of C shear texture irrespective of the initial textures and machining parameters. The result demonstrates that activations of slip systems and their relative activities depend on the shear deformation in machining of Ti-6AL-4V. This finding is important to control the texture variation in the deformation of Ti-6AL-4V.

Keywords: Crystallographic texture; VPSC simulation; Slip systems; OIM characterization; Machining; Ti-6AL-4V

1. Introduction

Crystallographic texture, induced by severe plastic deformation (SPD) of metal alloys, is a versatile route for amplifying mechanical properties and modulating functional responses [1-3]. Texture evolution of material is mainly controlled by the deformation fields (e.g. strain, strain rate, temperature) and the deformation modes (slip and twinning). Identifying the interconnections among the deformation fields, deformation modes and the texture evolution of materials is important to guide towards new ways of plastic deformation to control the texture of deformed materials.

Machining is a well-known SPD process that has been examined as one of the techniques of controlling/modifying textures of materials [4]. A schematic of machined surface formation during machining is illustrated in Fig. 1. By removing a preset depth of material a_0 , a chip of thickness of a_c and a new machined surface are generated. Large

amount of deformation is imposed in the primary deformation zone as the progression of cutting tool in the cutting speed direction. High strain rate (>10²), large strain (>1) and high temperature (>200 °C) result in reorientation tendencies of grains and thus a new crystallographic texture [5].

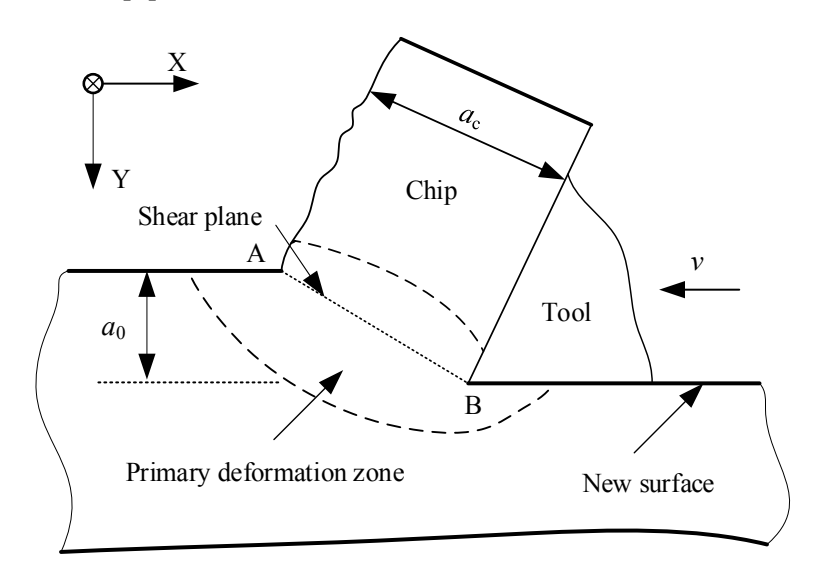


Fig. 1. Schematic of machining process.

Several studies have been conducted to identify and analyze the texture variations during machining of materials. Basu et al. used orientation imaging microscopy (OIM) to characterize the texture evolution of copper machined surfaces [6]. They also calibrated that visco-plastic self-consistent (VPSC) model can predict the texture variation during machining of copper. Velásquez et al. [7] found that the three types of texture were generated in the Ti-6AL-4V machined sub-surface. It was shown that it is possible to control the crystallographic texture variation by selecting proper cutting parameters.

Ti-6AL-4V, a typical dual-phase titanium alloy, was used in this paper. For the hexagonal close-packed (HCP) structure of α -Ti, five types of slip systems are involved in the SPD of Ti-6AL-4V, i.e., prismatic <a> {10-10}<11-20>, basal <a> {0002}<11-20>, pyramidal <a> {10-11}<11-20>, 1-st order pyramidal <c+a> {10-11}<11-23> and 2-nd

pyramidal $\langle c+a \rangle$ {11-22} $\langle 11-23 \rangle$. In addition to slip, Ti-6AL-4V shows a propensity for deformation twinning during SPD process. The twinning modes depend on the deformation characteristics of Ti-6AL-4V. Extension twinning mode {10-12} $\langle -1011 \rangle$ and compression twinning mode {10-11} $\langle 11-20 \rangle$ are the predominant twinning modes for HCP α -Ti.

Crystal plasticity theory has been used to establish the links between a set of slip/twinning systems activated in the deformation process of titanium alloy and the grain reorientations over the past several decades. Gurao et al. [8] showed that the activation of basal slip system is necessary to reproduce a near basal texture using VPSC model during room temperature compression of commercially pure titanium. In an analogous HCP system, Zecevic et al. [9] employed an elastic-plastic polycrystal model to elucidate the activities of 1-st pyramidal <c+a> and 2-nd pyramidal <c+a> slip systems on the effects of the texture variations during rolling of Mg-4%Li. The isolated effects of 1-st pyramidal <c+a> and 2-nd pyramidal <c+a> slip systems on grain reorientations were identified by using single-slip-mode within VPSC code. The studies mentioned above show that VPSC code can be used to discern which deformation modes are responsible for the texture variations during SPD of materials. However, there are few efforts that try to assess the relative activities of the multiple slip and twinning modes on the texture evolution during machining of Ti-6AL-4V [10].

In this work, a VPSC model with modified Voce type hardening was used to simulate texture evolution arising from different activated deformation modes during machining of Ti-6AL-4V. First, a finite element cutting simulation model was established to obtain the velocity vector fields in chips and machined surface during machining of Ti-6AL-4V. The

isolated effects of five slip families and one twinning mode on the texture variations with two initial textures were investigated via modifying the parameters in the Voce hardening of the VPSC code. Then, OIM analysis was performed to characterize the texture evolution in Ti-6AL-4V chips and machined surface. Eventually, slip or twinning systems were coupled and acted simultaneously with the VPSC simulated results agreeing well with the OIM experimental results. The calibrate VPSC model with modified Voce hardening parameters used to predict the crystallographic texture evolution during machining of Ti-6AL-4V was obtained.

2. VPSC simulation and experiments

2.1 VPSC model of texture simulation

In the present investigation, VPSC-7 code was used to simulate the texture evolution during machining of Ti-6AL-4V, in which each grain is assumed to be an ellipsoid, which is embedded in a homogeneous equivalent medium. The deformation of each grain is related with the macro deformation of polycrystal via physical shear mechanism of slip/twinning. A detailed description of the VPSC code can be found in the research of Tomé and Lebensohn [11].

Slip/twinning systems would be activated once the macro deformation is larger than the critical resolved shear stress (CRSS) of a certain slip/twinning system. Voce hardening scheme was used to update the CRSS evolution of slip/twinning system with respect to the accumulated shear strain. This is expressed as Eq. (1).

$$\tau^{s} = \tau_{0}^{s} + \left(\tau_{1}^{s} + \theta_{1}^{s}\Gamma\right)\left(1 - \exp\left(-\Gamma\left|\frac{\theta_{0}^{s}}{\tau_{1}^{s}}\right|\right)\right)$$

$$\tag{1}$$

where τ_0 , θ_0 , θ_1 , $(\tau_0+\tau_1)$ are the initial CRSS, the initial hardening rate, the asymptotic

hardening rate and the back-extrapolated CRSS, respectively. Γ is the accumulated shear strain in the grain. The plastic strain rate in single crystal level associated with the shear strain is given by Eq. (2). It can also be rewritten in a linear form.

$$\dot{\varepsilon}_{k} = \dot{\gamma}_{0} \sum_{s=1}^{S} m_{k}^{s} \left(\frac{m_{j}^{s} \sigma_{j}^{\prime}}{\tau^{s}} \right)^{n'} = M_{ij}^{c(\text{sec})} (\sigma^{\prime}) \sigma_{j}^{\prime}$$
(2)

where $M_{ij}^{c(\text{sec})}(\sigma')$ and σ'_j are the viscoplastic compliance and the local deviatoric stress term of grain, respectively. n' is the inverse of strain rate sensitivity exponent. For the self-consistent process, it is assumed that the strain rate in each grain equals to the polycrystal macroscopic strain rate [11].

Arbitrary Lagrange-Euler (ALE) algorithm with Abaqus/Explicit was used to develop Ti-6AL-4V cutting simulation model. The detailed procedures of the implementation and the validation of the Ti-6AL-4V cutting simulation model were presented in our previous research [12]. Johnson-Cook (J-C) constitutive model, as expressed with Eq. (3), was used to define Ti-6AL-4V dynamic behavior during machining process.

$$\sigma = \left(A + B\varepsilon^{n}\right)\left[1 + C\ln\left(\frac{\dot{\varepsilon}}{\dot{\varepsilon}_{0}}\right)\right]\left[1 - \left(\frac{T - T_{r}}{T_{m} - T_{r}}\right)^{m}\right]$$
(3)

in which A, B, C, n, m are J-C material parameters for Ti-6Al-4V. Strain rate sensitivity proportional factors in J-C constitutive model and VPSC model are defined with Eqs. (4) and (5), respectively.

$$\frac{\sigma(\dot{\varepsilon})}{\sigma(\dot{\varepsilon}_0)} = 1 + C \ln \left(\frac{\dot{\varepsilon}}{\dot{\varepsilon}_0}\right) \tag{4}$$

$$\frac{\sigma(\dot{\varepsilon})}{\sigma(\dot{\varepsilon}_0)} = \left(\frac{\dot{\varepsilon}}{\dot{\varepsilon}_0}\right)^{\frac{1}{n'}} \tag{5}$$

in which the referenced strain rate $\dot{\varepsilon}_0$ is 0.0001 s⁻¹. The strain rate is ranged from 0.0001 s⁻¹

to $10000s^{-1}$. As shown in Fig. 2, the inverse of strain rate sensitivity exponent n' in VPSC model is set as 44 to coincide with the material behavior predicted using J-C constitutive model (with the value of C 0.028).

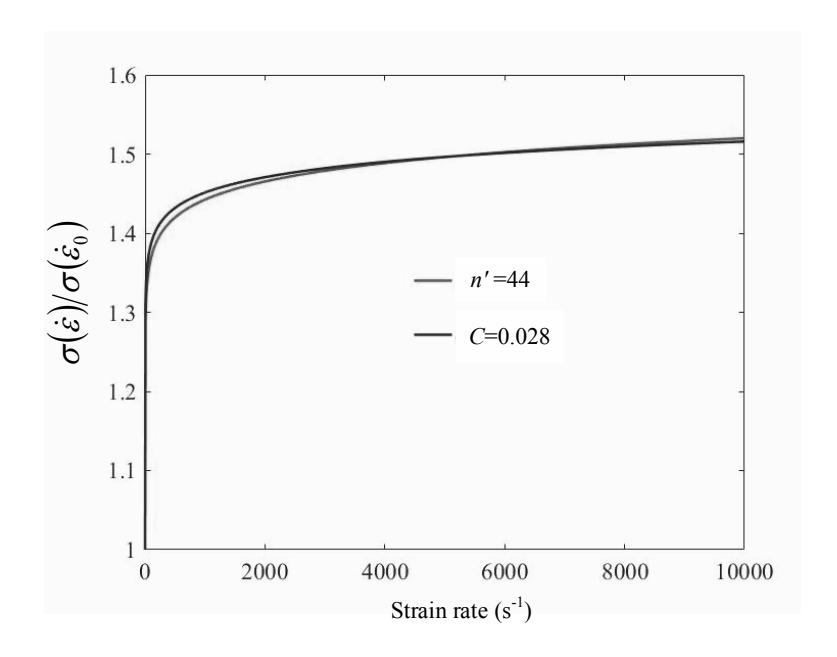


Fig. 2. Strain rate sensitivity proportional factors of J-C constitutive model and VPSC model.

Two deformation paths were defined in the machining process of Ti-6AL-4V, as shown in Fig. 3. Deformation path A entered into chip and deformation path B became part of machined subsurface. Strain field, strain rate field and deformation gradient of defined deformation paths were extracted from the established cutting simulation model. Velocity gradients of deformation paths A and B were calculated based on the presented outputs of Ti-6AL-4V machining process.

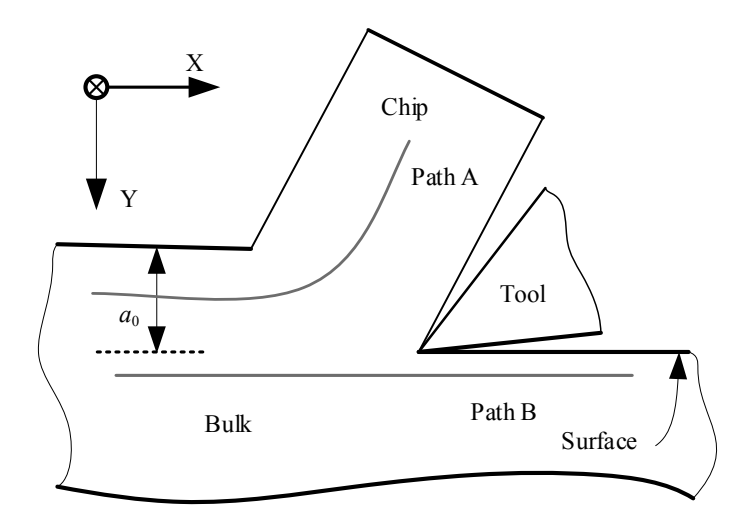


Fig. 3. Deformation paths defined in the machining of Ti-6AL-4V.

Two initial texture distribution data sets of as-received state without any additional annealing and with post annealing were used in the texture simulations. The simulated texture data were analyzed using MTEX software [13]. Based on our previous research, only one twinning deformation mode {10-11}<11-20> was generated during machining of Ti-6AL-4V [14]. Therefore, the Voce hardening law parameters for all slip systems and associated with the twinning mode of {10-11}<11-20> of Ti-6AL-4V were adjusted. It is possible to control the activation of each deformation mode and characterize its effects on texture variation in machining of Ti-6AL-4V. Relative amount of shear contributed by each deformation mode in every deformation step was available in the VPSC output files. Various deformation modes were combined by modifying the Voce hardening parameters and the relative contributions of each deformation mode on the texture variation were estimated.

In this work, Voce hardening parameters were modified based on the research of Galán-López and Verleysen [15]. The values for Voce hardening parameters are tabulated in Table 1. Self and latent hardening parameters for 4 slip systems were equal to 1, to avoid introducing strong and unpredictable coupling effects between various slip systems [16]. The

values of θ_1 for all the slip systems were set to 0 to reduce the parameters optimization time in Voce hardening law [18]. It should be noted the activated sequences of slip systems are prismatic, basal, pyramidal <a>a>, 1-st pyramidal <c+a>. They demonstrated the fitting parameters can be successfully applied to simulate texture evolution during large deformation of Ti-6AL-4V. However, second-order pyramidal <c+a> slip system and deformation twinning modes were not considered in their research.

Table 1 Voce hardening parameters for 4 slip systems of α titanium [15].

Deformation mode	Prismatic	Basal	Pyramidal <a>	Pyramidal <c+a></c+a>
τ_0 (MPa)	290.8	411.5	506.6	654.1
τ_1 (MPa)	126.0	205.5	408.5	700.2
θ_0 (MPa)	113.6	167.0	394.1	970.0

2.2 Machining experiments and texture measurements

The Ti-6AL-4V used in this study is composed about of 90% by volume of HCP α -phase and 10% of body-centered cubic (BCC) β -phase. Plastic deformation of Ti-6AL-4V in this study relies predominantly on the slip of HCP α -Ti. Orthogonal cutting tests of Ti-6AL-4V with two initial textures were conducted on lathe to obtain new generated machined surface and chips. As described in Fig. 3, the depth of cut a_0 was set to 100 μ m. High speed steel cutting tool was used. The tool rake angle was selected as 5°. Two cutting speeds of 550 mm/s and 1100 mm/s were used in the machining tests. OIM characterizations of the machined surface and chips were performed in a FEI SciosTM ultra-high-resolution analytical DualBeam system equipped with electron back-scattered diffraction (EBSD) detector. To eliminate the effect of initial texture on the experimental results, all the characterized areas of

EBSD were maintained on the cross-section of Ti-6AL-4V cylindrical samples (Fig. 4). The examined samples were prepared with mechanical grinding first and final polishing in a 0.04 µm colloidal silica suspension for about 1 hour. EBSD was operated in a voltage of 20 kV and a beam spot size of 13 - 15 (current strength about 5 - 7 nA).

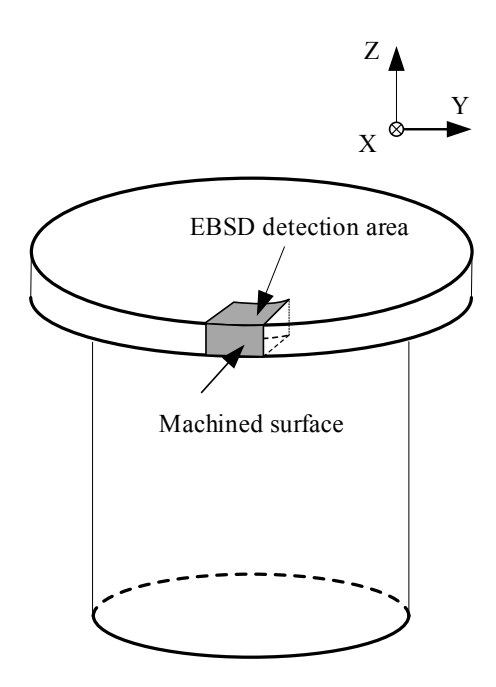


Fig. 4. Schematic of EBSD detection area of Ti-6AL-4V.

3. Results

3.1 Initial textures of Ti-6AL-4V

Fig. 5 shows the initial texture of Ti-6AL-4V bar without post annealing. The detection area was perpendicular to the axis of Ti-6AL-4V bar. Pole figures (PFs) (Fig. 5(c)) and inverse pole figures (IPFs) (Fig. 5(b)) present that the main texture component of Ti-6AL-4V is {11-20}<0001>. Likewise, the initial texture of Ti-6AL-4V with post annealing is presented in Fig. 6. A new texture component of {10-10}<0001> is generated. Both the PFs and IPFs of two initial Ti-6AL-4V alloys also reveal a very weak basal sheet texture {0001}. Besides, the average grain size of Ti-6AL-4V with post annealing is larger than that without post annealing as full recrystallization was occurred with post annealing.

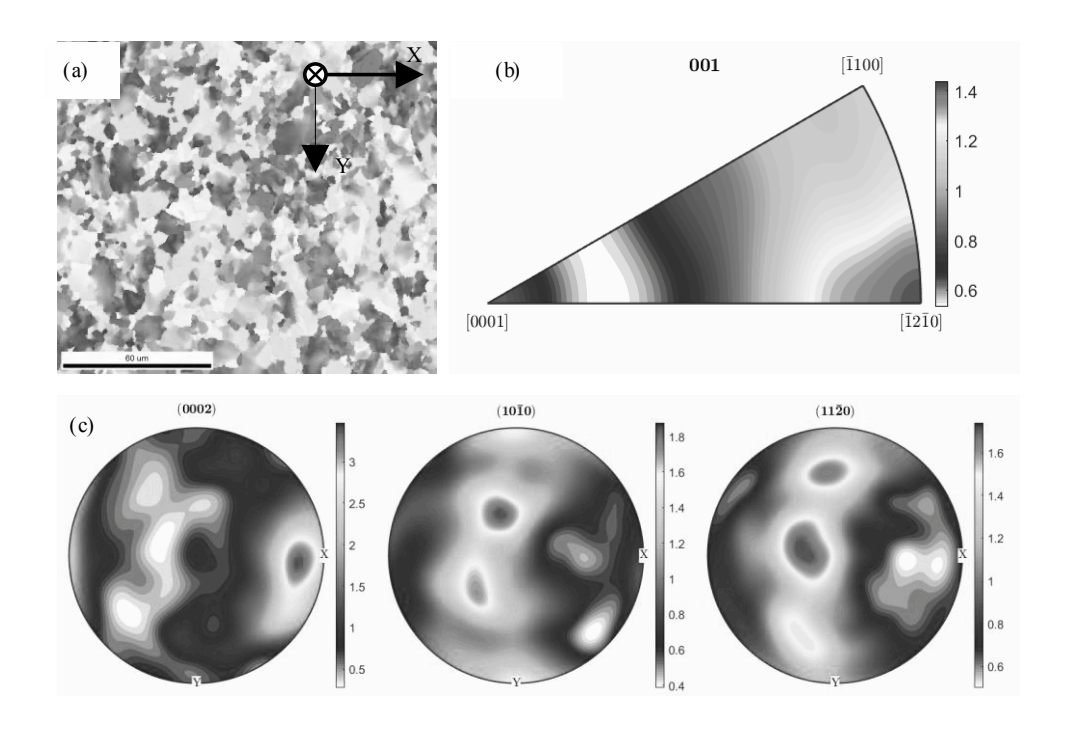


Fig. 5. Initial texture component of Ti-6AL-4V in the as-received state without any additional annealing.

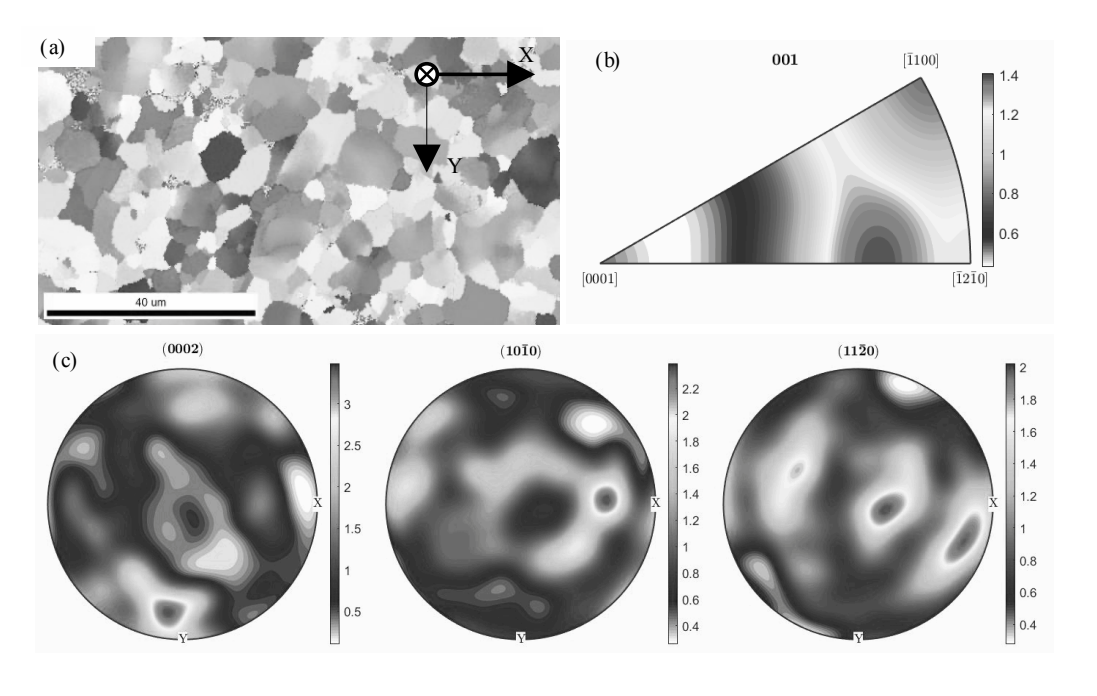


Fig. 6. Undeformed initial texture component of Ti-6AL-4V after annealing of the bulk.

3.2 Texture variations in chips and machined surface with two initial materials

The crystallographic texture variations of Ti-6AL-4V machined surface created from bulk in the as-received state at cutting speeds of 550 mm/s, and 1100 mm/s are shown in Fig. 7 and Fig. 8, respectively. Orientation distribution function (ODF) maps were established

with Bunge system angles (φ_1 , Φ) restricted to a region { $\pi/2$, $\pi/2$ } and angle φ_2 was sectioned into 6 parts (0°, 10°, 20°, 30°, 40°, 50°) for the symmetry of textures of hexagonal materials. A typical shear texture, C fiber shear texture is seen from the PFs. The ideal positions of C fiber are simple points in the {0002} PF and lines in both the {10-10} and {11-20} PFs [18]. The texture component is approximately specified by the Euler angles (60°, 90°, 0-60°) by analyzing the ODF maps.

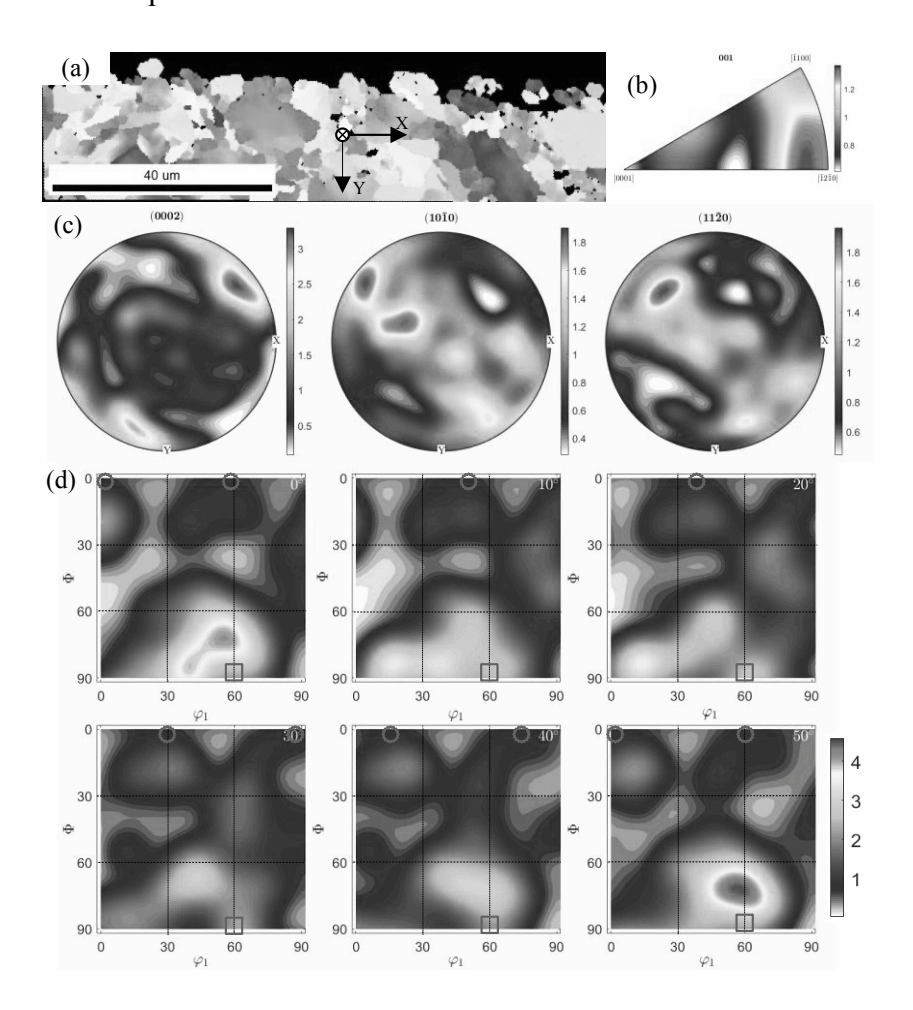


Fig. 7. Texture variations of Ti-6AL-4V machined surface created from bulk in the as-received state at cutting speed of 550 mm/s. (a) IPF map; (b) IPF; (c) PFs; (d) ODF maps. Symbols "□" and "○" represent texture components of C fiber shear texture and basal sheet texture {0001}, respectively.

Besides, the weak basal sheet texture {0001} is still maintained in the machined surface under both cutting speeds. Two basal sheet texture components {0001}<11-20> and

 $\{0001\}$ <10-10> are detected in the ODF maps. They are specified by the Euler angles $(\varphi_2+\varphi_1=30^\circ, 0^\circ, \varphi_2+\varphi_1=30^\circ)$ and $(\varphi_2+\varphi_1=60^\circ, 0^\circ, \varphi_2+\varphi_1=60^\circ)$, respectively, marked with circles as shown in Figs. 7(d) and 8(d). It can also be seen that the intensity of basal texture is strengthened at cutting speed of 1100 mm/s compared with that at cutting speed of 550 mm/s. At the same time, weak bulk texture component of $\{11-20\}$ <0001> is detected in the machined surface at the cutting speed of 1100 mm/s. The ideal location of bulk texture is specified by Euler angles $(90^\circ, 90^\circ, 0/60^\circ)$ marked with triangle in Fig. 8(d).

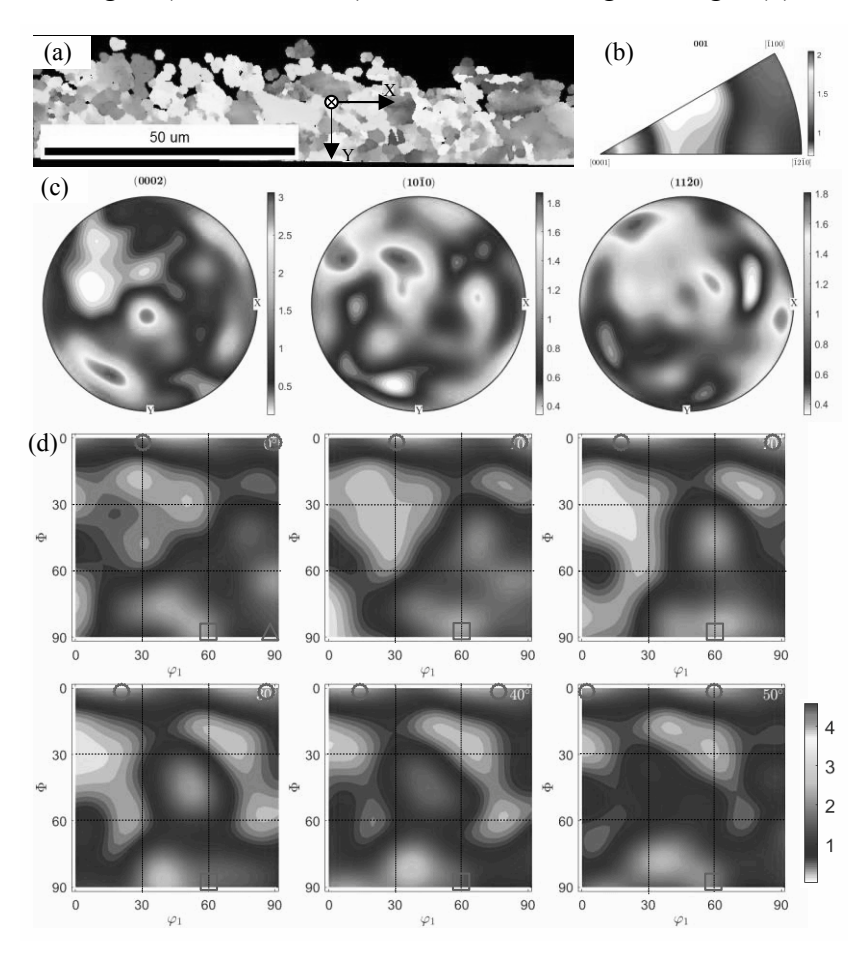


Fig. 8. Texture variations of Ti-6AL-4V machined surface created from bulk in the as-received state at cutting speed of 1100 mm/s. (a) IPF map; (b) IPF; (c) PFs; (d) ODF maps. Symbols "△, □, and ○" represent texture components of {11-20}<0001>, C fiber shear texture and basal sheet texture {0001}, respectively.

Figs. 9 and 10 show the texture evolution of Ti-6AL-4V machined surface, which were created on the sample, which was annealed in the bulk state. The detection area at cutting speed of 1100 mm/s, is opposite to that under other cutting conditions, as shown in Fig. 10(a), the X axis of spatial reference system is the same direction with cutting speed, which is opposite to that in Figs. 7(a), 8(a) and 9(a). ODF maps in Fig. 10(d) are restricted to the Euler angles of (60-150°, 0-90°, 0-60°). Both the PFs and ODF maps reveal that the main texture component is C fiber shear texture. It is specified by the Euler angles of (120°, 90°, 0-60°), which is the same location with that (60°, 90°, 0-60°). There is a little deviation between the detection locations in Fig. 9(d) and the ideal locations of C fiber shear texture.

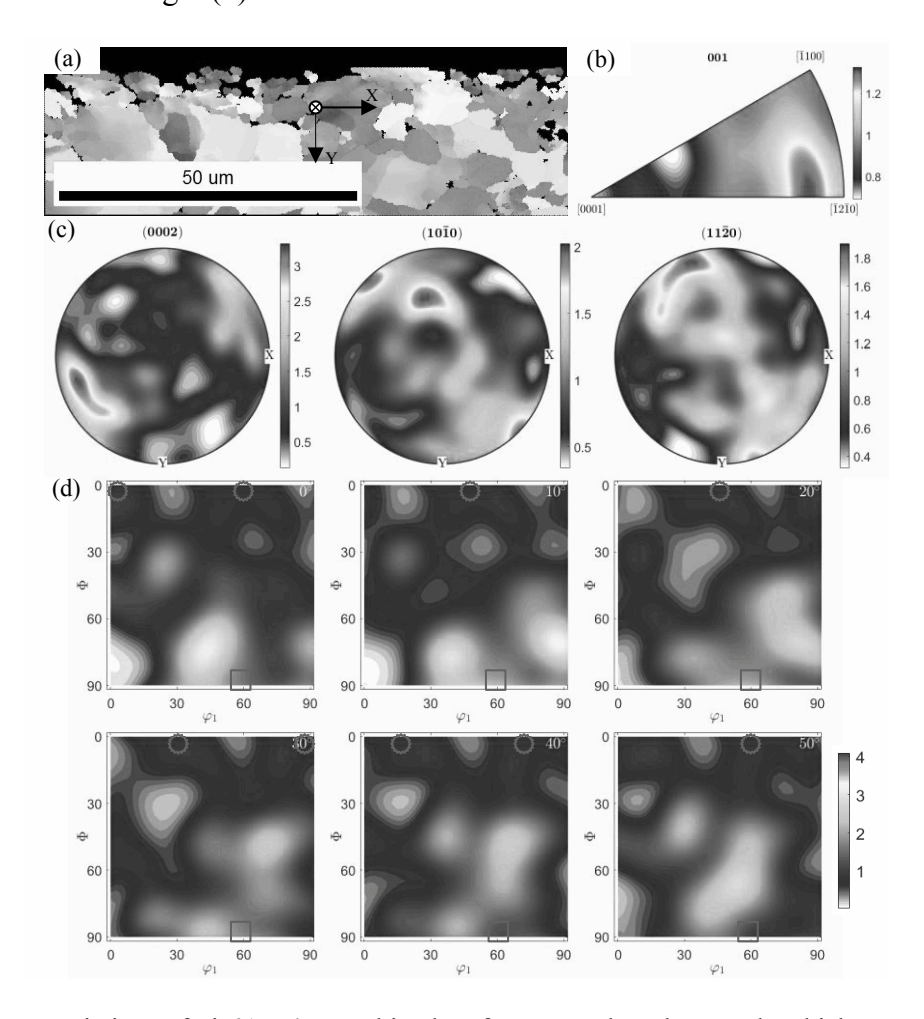


Fig. 9. Texture variations of Ti-6AL-4V machined surface created on the sample which was annealed in the bulk state at cutting speed of 550 mm/s. Symbols "□" and "○" represent texture components of C

fiber shear texture and basal sheet texture {0001}, respectively.

Additionally, similar observations are obtained for the basal sheet texture component $\{0001\}$ in Ti-6AL-4V machined surface compared with Figs. 7 and 8. The ideal locations are specified with the Euler angles $(\varphi_1+\varphi_2=60^\circ, 0^\circ, \varphi_1+\varphi_2=60^\circ)$ and $(\varphi_1+\varphi_2=150^\circ, 0^\circ, \varphi_1+\varphi_2=150^\circ)$. The measured intensity values are present near the ideal locations of basal sheet texture $\{0001\}$. Initial bulk texture component $\{10-10\}<0001>$ is also characterized in the ODF maps, marked with triangles. The ideal locations are specified by the Euler angles $(90^\circ, 60^\circ, 0-60^\circ)$ [19]. Similar results are observed compared with Fig. 8 that the intensity of bulk texture component is increased at cutting speed of 1100 mm/s.

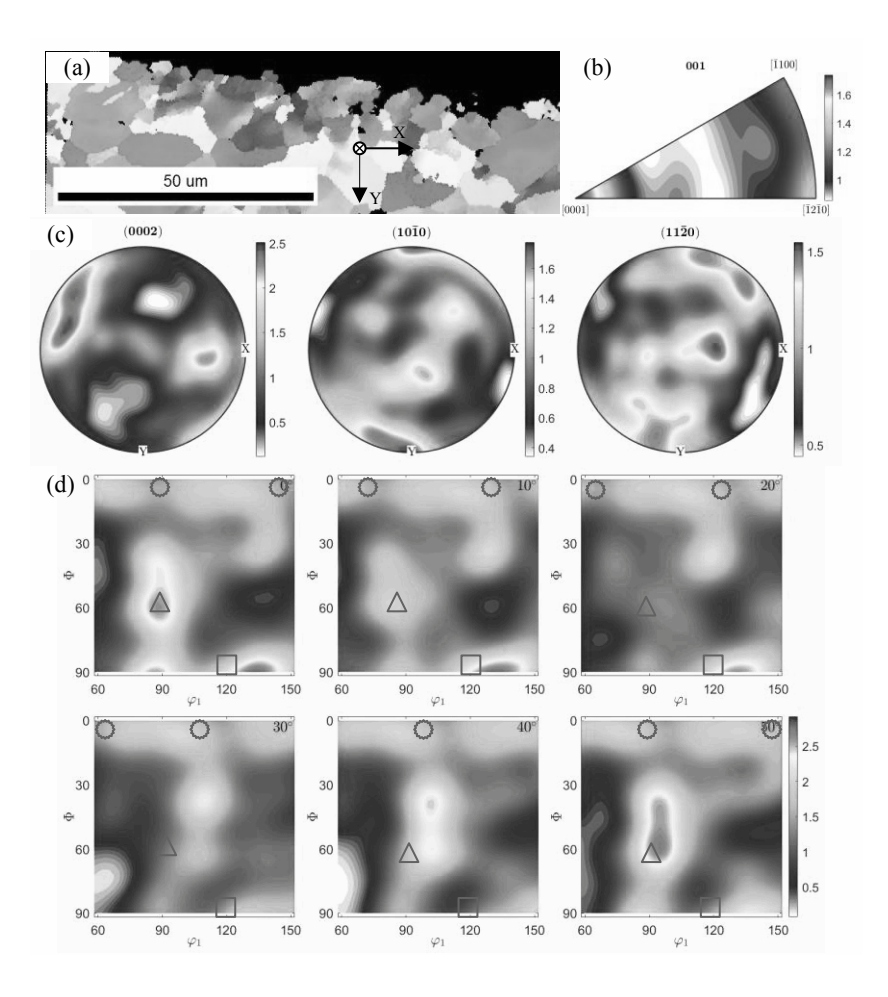


Fig. 10. Texture variations of Ti-6AL-4V machined surface created on the sample which was annealed in the bulk state at cutting speed of 1100 mm/s. Symbols " \triangle , \square , and \bigcirc " represent texture components of

{10-10}<0001>, C fiber shear texture and basal sheet texture {0001}, respectively.

Chips at cutting speed of 1100 mm/s was selected as a representative case and the texture evolution is presented in Fig. 11. PFs were plotted referring to shear plane AB as described in Fig. 1. It is evident from Figs. 11(a) and 11(e) that serrated chips are formed and the grains in the shear bands are severely elongated in the shear direction. There are slight differences of the texture locations in the PFs and ODF maps along deformation paths A and B. The generated texture along deformation path A is specified by Euler angles (30°, 90°, 0-60°). Corresponding changes of texture locations can be observed in the PFs. Actually, the generated texture type along deformation path A is the same as that along deformation path B. However, the texture intensity along deformation path A is stronger than that along deformation path A is much severer than that along deformation path B.

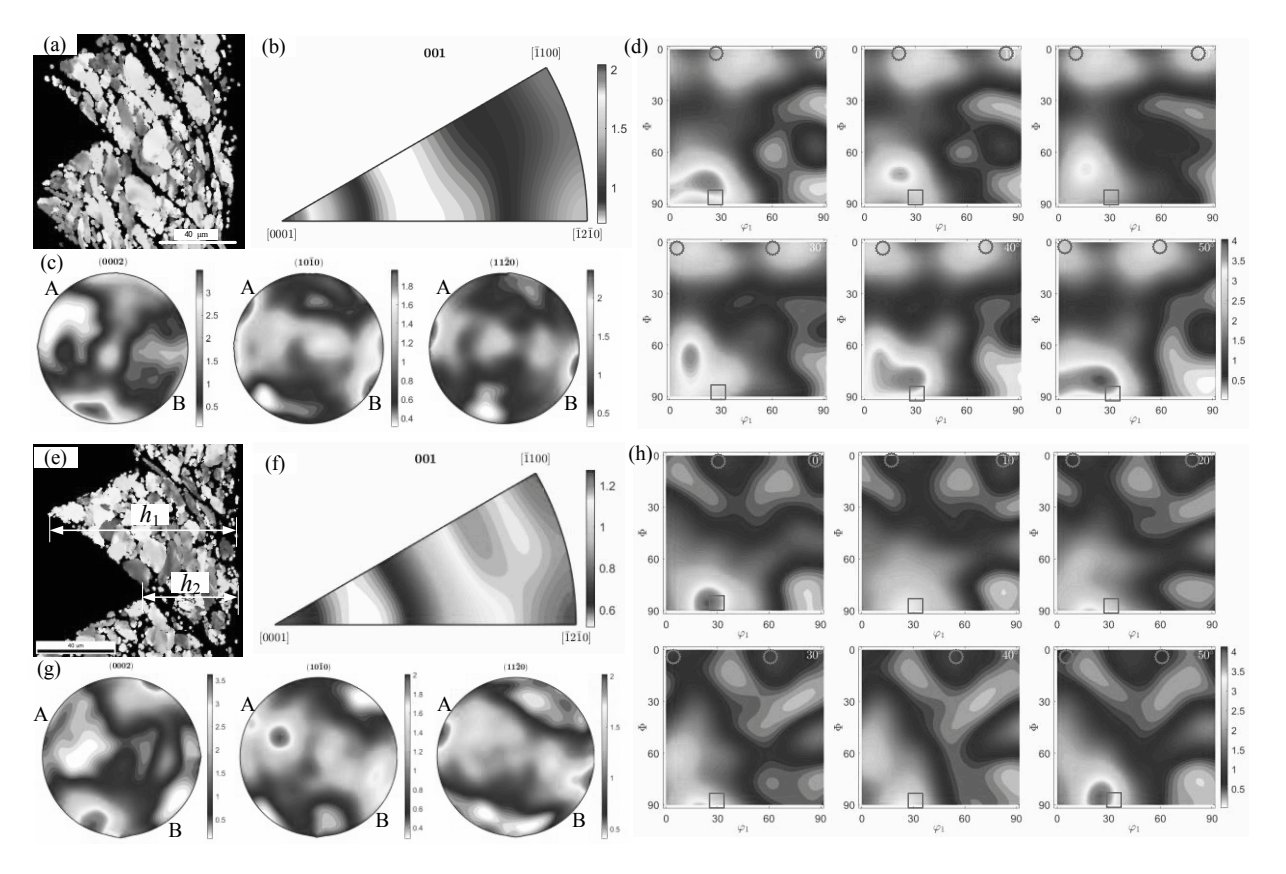


Fig. 11. Texture variations of Ti-6AL-4V chips at cutting speed of 1100 mm/s. (a) - (d) created from bulk in the as-received state; (e) - (h) created on the sample which was annealed in the bulk state. Symbols "□" and "○" represent texture components of C fiber shear texture and basal sheet texture {0001}, respectively.

Compared with chips created at a cutting speed of 1100 mm/s from the as-received bulk without an annealing treatment, the intensity of basal sheet texture $\{0001\}$ is weaker in the samples created at cutting speed of 1100 mm/s from the bulk material, which was annealed. The difference indicates that deformation modes activated during machining and contributions to the formation of texture components are different. It is seen that chip morphologies (chip peak h_1 and chip valley h_2) are different in the two cutting conditions. Deformation in two types of chips is directly related with chip morphologies. It is deduced that the extent of deformation in chips determines the intensity of generated basal sheet texture $\{0001\}$. We will discuss it in Section 4.2 of this work.

3.3 Deformation histories during machining of Ti-6AL-4V

Strain and strain rate tensors at each point of machined area are simplified as $\begin{pmatrix} \varepsilon_{xx} & \varepsilon_{xy} \\ \varepsilon_{yx} & \varepsilon_{yy} \end{pmatrix}$ and $\begin{pmatrix} \dot{\varepsilon}_{xx} & \dot{\varepsilon}_{xy} \\ \dot{\varepsilon}_{yx} & \dot{\varepsilon}_{yy} \end{pmatrix}$ since machining process coincided with plane strain conditions.

Fig. 12 shows the simulated results of effective strain and shear strain rate distributions during machining of Ti-6AL-4V. As an ALE framework was used in the cutting simulation model, there is a big difference between the simulated chip morphologies and the experimental results. However, large amount of deformation is imposed in the primary deformation zone and the material becomes chips and machined surface. The deformation in a shear band was extracted and the strain and strain rate fields along deformation path A can

be simulated accurately.

Strain variation is an accumulative process, so the effective strain value in the primary deformation zone, as shown in Fig. 12(a), is not large. On the contrary, high strain rate is located in the primary deformation zone since strain rate is a measure of strain imposed per unit time. Fig. 12(b) shows the shear strain rate distribution contour. It is evident that high strain rate distribution zone is the primary deformation zone.

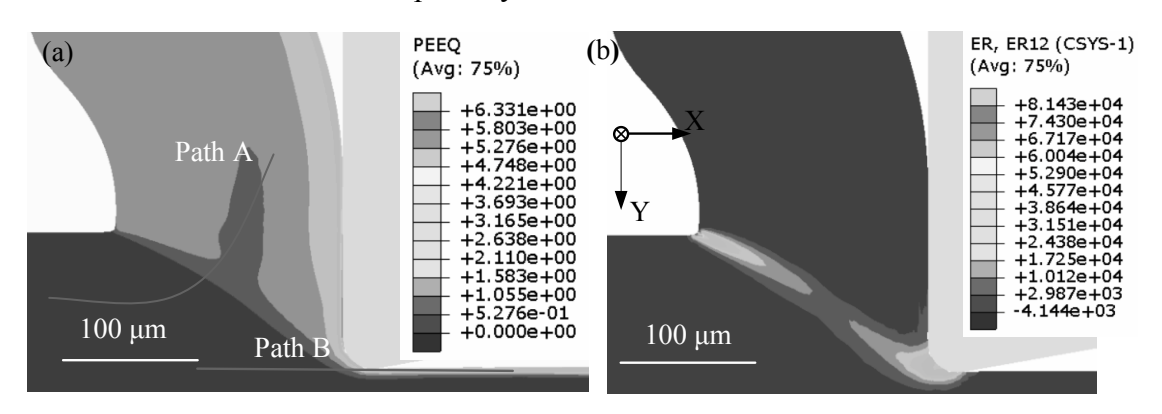


Fig. 12. Deformation histories during machining of Ti-6AL-4V at cutting speed of 550 mm/s. (a) Effective strain field; (b) Shear strain rate.

Variations of effective strain and shear strain rate along defined deformation paths with cutting time are plotted in Fig. 13. Effective strain along paths A and B (Fig. 13(a)) increase rapidly with cutting time and then gradually tends to attain saturation values. It is indicated that the variation of effective strain is an accumulative process. The saturation values of effective strain reveal that the deformation of material is ceased. And, the distributions of shear strain rate along deformation paths present unimodal distribution with cutting time. The peak values are located in the primary deformation zone. Strain rate histories along deformation paths A and B are consistent with the strain histories. The simulated distributions of strain, strain rate along deformation paths A and B are agreed well with the measured results of Guo et al. [20]. Coupled with the deformation gradient along the deformation paths,

velocity gradient are obtained and inputted into the VPSC simulation code.

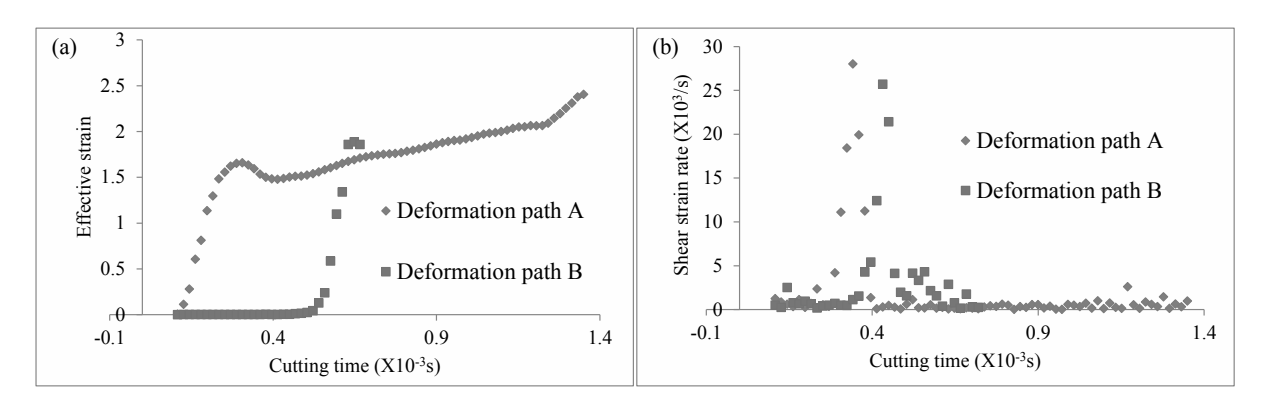


Fig. 13. Evolutions of effective strain and shear strain rate along deformation paths A and B at cutting speed of 550 mm/s. (a) Effective strain; (b) Shear strain rate.

The cutting temperature variations during machining of Ti-6AL-4V are also analyzed and are shown in Fig. 14. It is seen from Fig. 14(a) that the highest temperature is located in the chip - tool rake face contract zone. The cutting temperature along deformation path B at cutting speed of 550 mm/s is plotted in Fig. 14(b). It is evident that the cutting temperature is an accumulative process during machining of Ti-6AL-4V. With the continuous progression of cutting tool, the cutting temperatures in chip and the machined surface are decreased. It has been proved that high temperature can reduce the CRSS values of slip systems and thus promote the activations of slip systems [21]. To couple the high cutting temperature effect in the Voce hardening law of VPSC model, the initial CRSS values of slip systems were reduced in certain degrees. The modified Voce hardening parameters of slip systems will be given in Section 4.1 of this study.

deformation twinning system

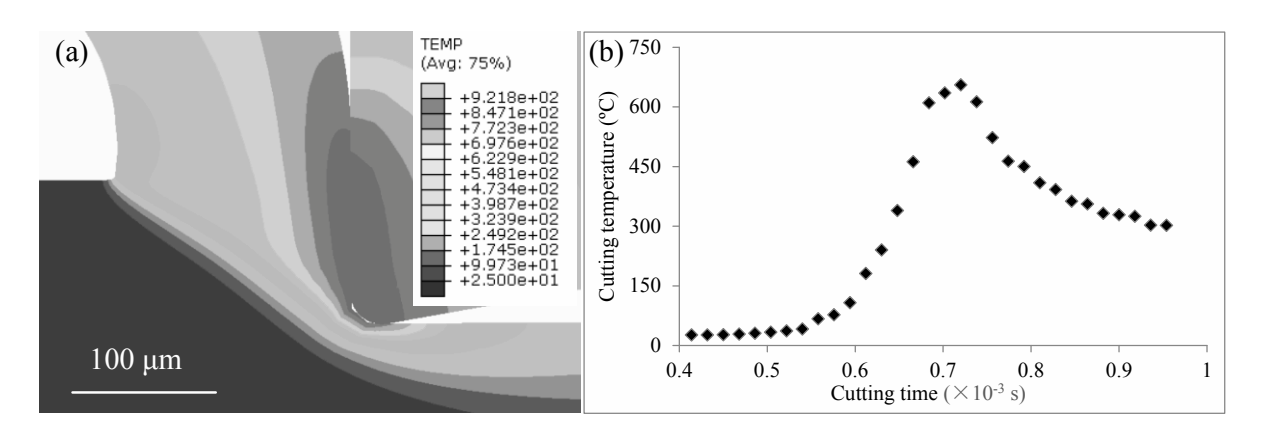


Fig. 14. Variation of cutting temperature during machining of Ti-6AL-4V at cutting speed of 550 mm/s. (a)

Cutting temperature distribution contour; (b) Cutting temperature distribution along deformation path B.

3.4 VPSC simulation results of different activated slip systems and associated with one

Initial orientation data from the as-received bulk without any annealing was selected as a representative case. The isolated contributions of 5 slip systems and deformation twinning mode to the texture variations along deformation path B at cutting speed of 550 mm/s were obtained by modifying Voce hardening parameters. Prismatic slip mode is the first to be activated during deformation of α titanium material. Fig. 15 shows the texture variations when only prismatic slip system is activated. It is evident that the locations of these most active prismatic slip orientations are very similar to the split basal peak texture developed in the stable rolled textures of Mg alloys [19]. The ideal locations of basal sheet texture {0001} are marked in Fig. 15(c) with circles. The generation of basal sheet texture {0001} reveals that prismatic slip mode is responsible for the rotation of {10-10} prismatic plane in the normal compression/tension stress direction in the primary deformation zone [22].

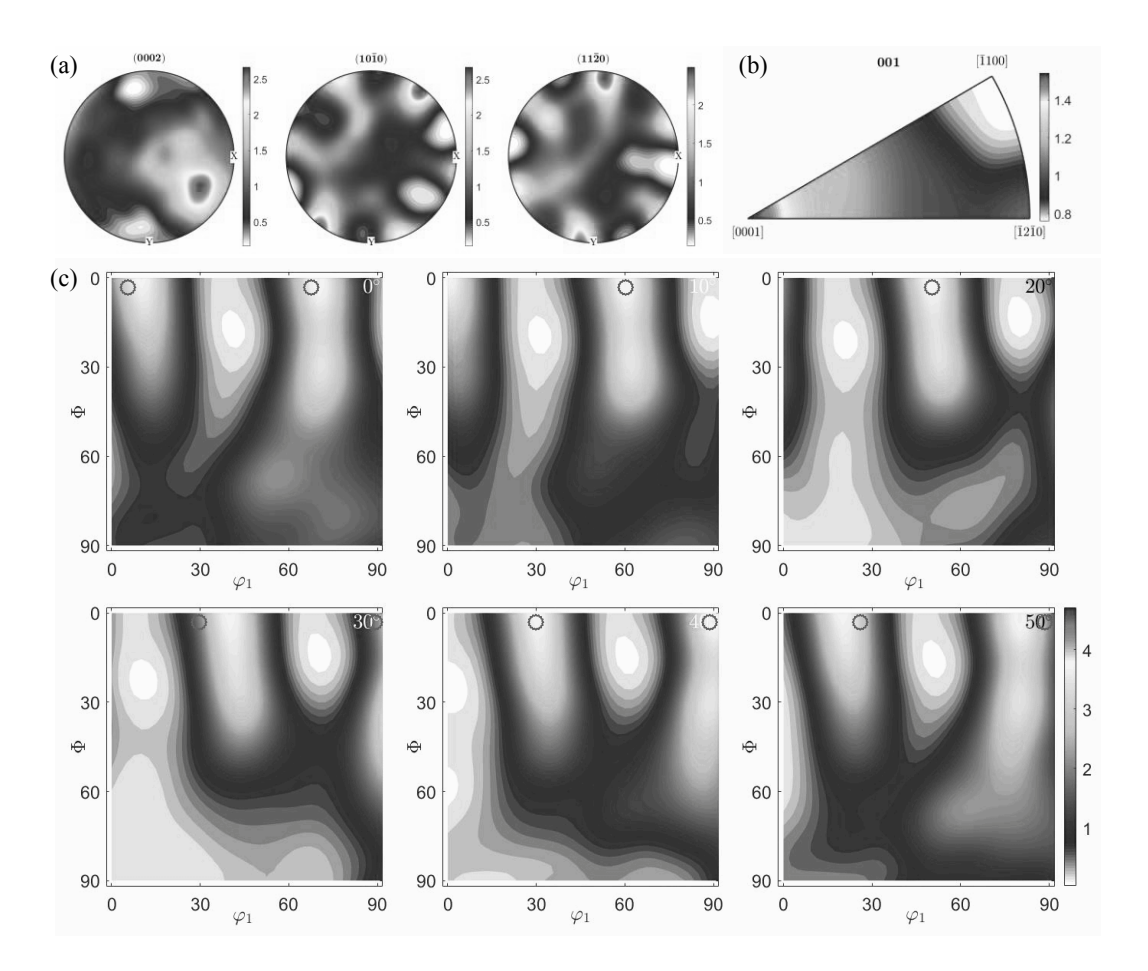


Fig. 15. Texture variations along deformation path B at cutting speed of 550 mm/s with only prismatic slip mode activated. (a) PFs; (b) IPF in Z direction; (c) ODF maps. Symbol "O" represents basal sheet texture {0001}.

Fig. 16 shows the texture evolution with the activity of basal slip system. ODF maps in Fig. 16(c) expose the generated texture component is (150°, 90°, 0-60°) when only basal slip mode is activated. This texture is similar to B fiber shear texture generated in equal channel angular pressing (ECAP) of magnesium [23]. The ideal locations of B fiber shear texture of magnesium characterized by Euler angles are (45°, 90°, 0-60°). The difference in φ_1 angle is presumably due to the distinct shear deformation during machining of Ti-6AL-4V.

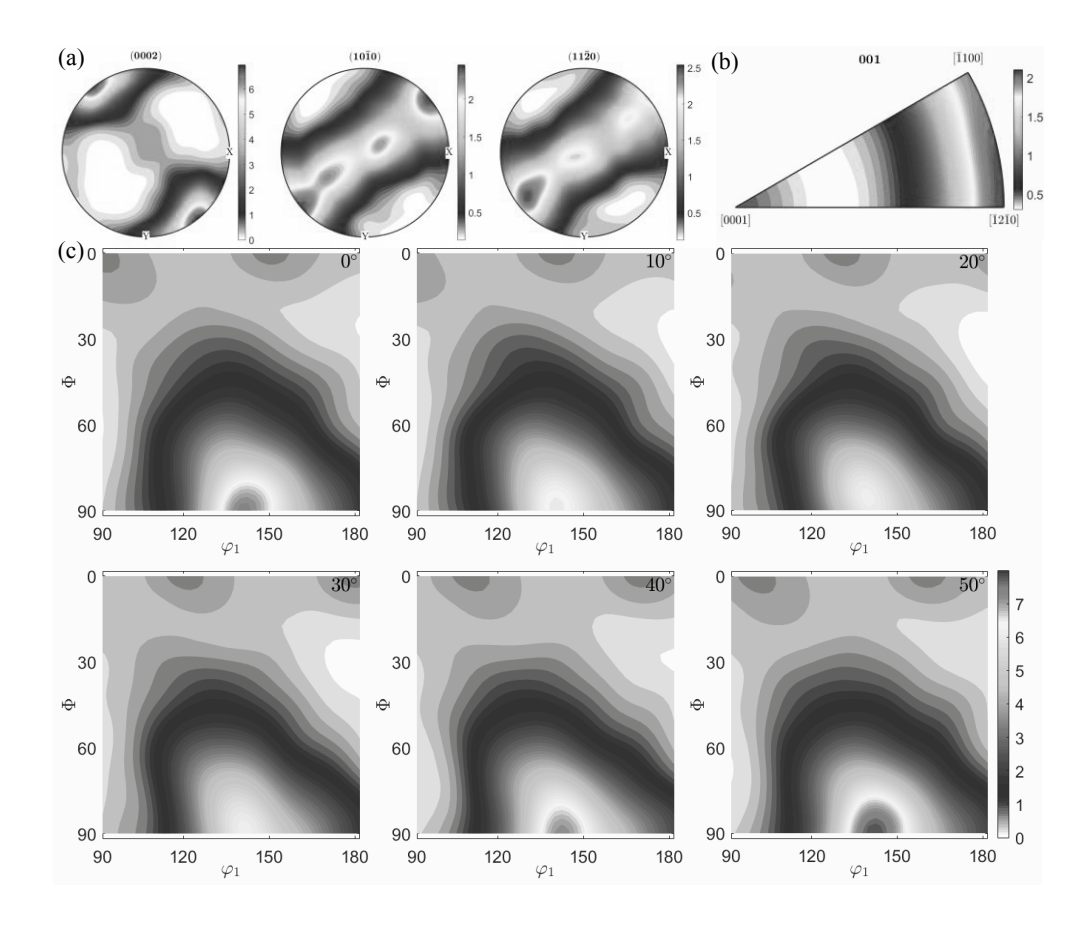


Fig. 16. Texture variations when only basal slip mode is activated. (a) PFs; (b) IPF in Z direction; (c) ODF maps.

The texture variation with the activity of pyramidal <a> slip system is shown in Fig. 17. ODF maps in Fig. 17(c) reveal the texture component is (150°, 60°, 0-60°). It is obvious that the ϕ angle is rotated 30° compared with that only basal slip mode is activated. Correspondingly, in the IPF of Fig. 17(b), texture intensity changes from [-12-10] direction to [10-10] direction. There is also a change in φ_1 angle compared with the bulk texture component (90°, 90°, 0/60°). Or, we can say the texture variation with the activation of pyramidal <a> slip mode is based on the texture variation with the activation of basal slip mode. Pyramidal <a> slip mode first generates a rotation of c axis towards Z-X plane and then towards Z direction. Compared with the OIM analysis results, it is concluded that the simulated results do not agree well with the experimental results when only prismatic and

basal slip systems are activated.

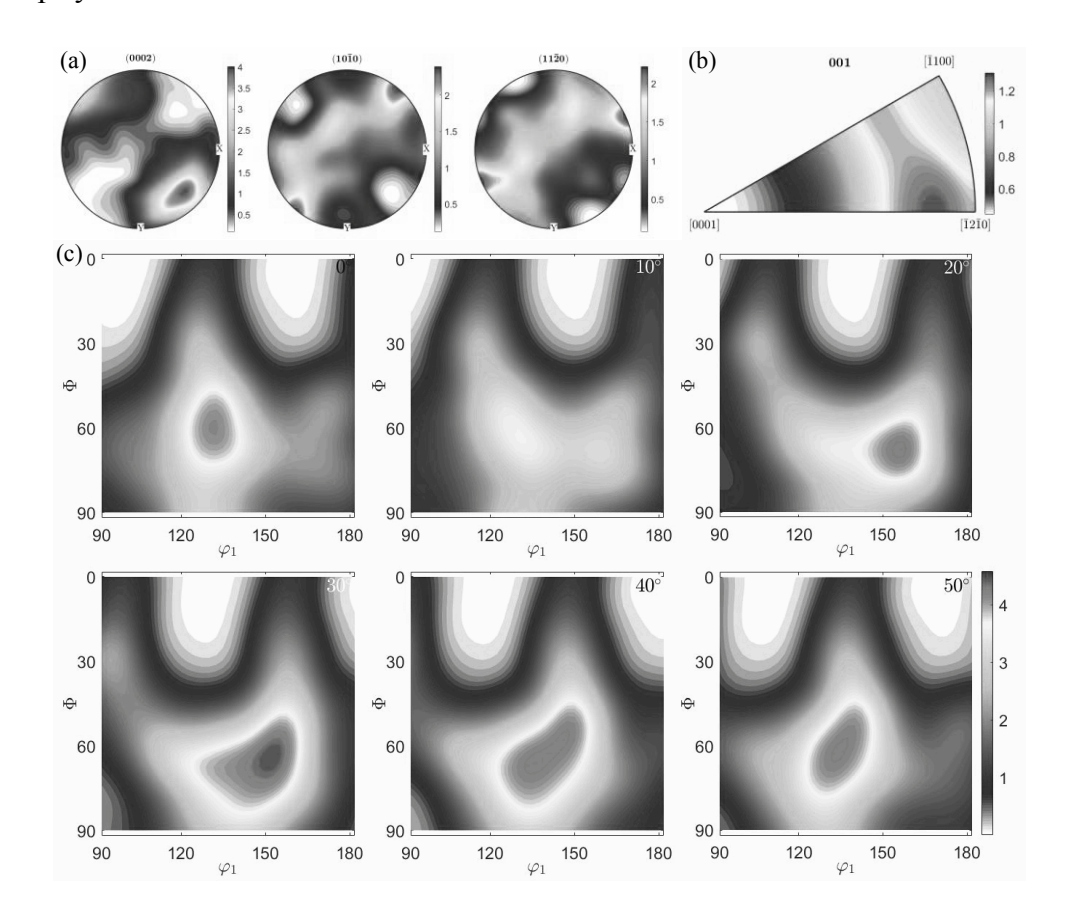


Fig. 17. Texture variation when only pyramidal <a> slip mode is activated. (a) PFs; (b) IPF in Z direction; (c) ODF maps.

Figs. 18 and 19 present the texture variations with the activities of 1-st order pyramidal <c+a> slip mode and 2-nd order pyramidal <c+a> slip mode. Both the ODF maps in Fig. 18(c) and 19(c) present the texture components locations are (60°, 90°, 0-60°). It is hard to characterize the texture variations with the activities of 1-st order pyramidal <c+a> slip mode and 2-nd order pyramidal <c+a> slip mode from the ODF maps. There are slight differences in the {10-10} and {11-20} PFs as shown in Figs. 18(a) and 19(a). Unlike 1-st order pyramidal <c+a> slip, 2-nd order pyramidal <c+a> slip favors formation of four peaks in {10-10} PF. Gajewska et al. [24] also detected the intense texture component during ECAP process of commercially pure titanium is located at the same positions as in Fig. 19(a). It is

concluded that 2-nd order pyramidal <c+a> slip mode shows better capability of reproducing texture features during machining of Ti-6AL-4V.

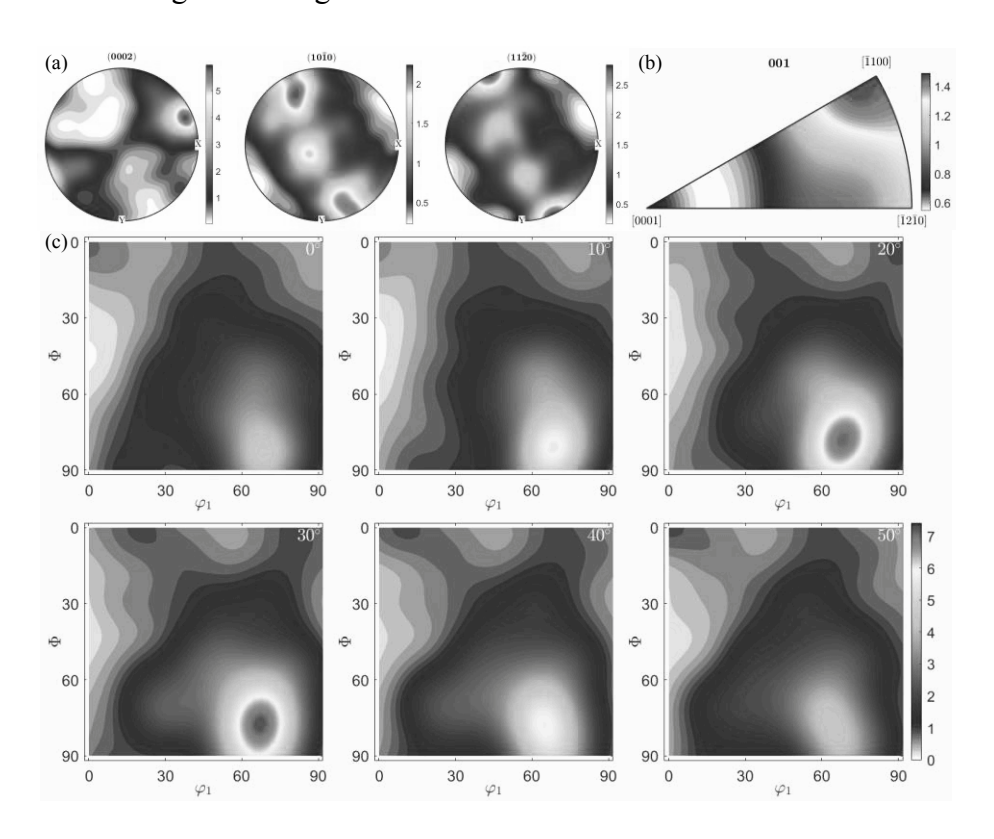


Fig. 18. Texture simulated results when only 1-st order pyramidal <c+a> slip mode is activated. (a) PFs; (b)

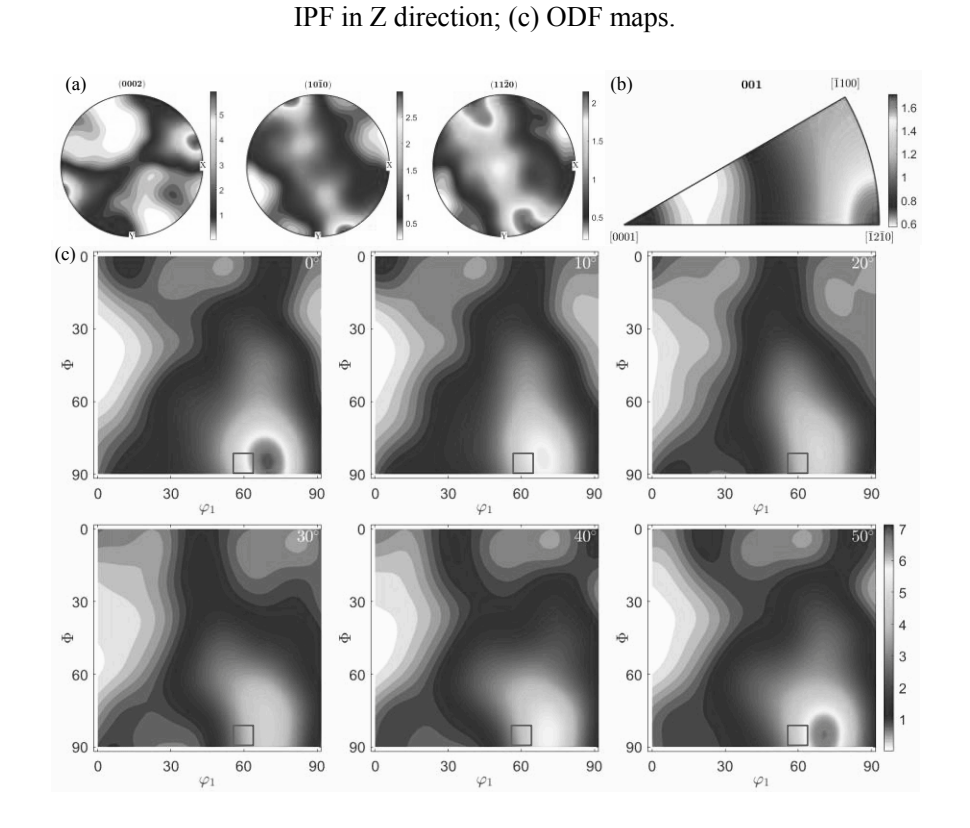


Fig. 19. Texture simulated results when only 2-nd order pyramidal <c+a> slip mode is activated. (a) PFs; (b) IPF in Z direction; (c) ODF maps. Symbol "□" represents C fiber shear texture.

Texture simulation result when only one deformation twinning mode $\{10\text{-}11\}<10\text{-}12>$ is activated is shown in Fig. 20. The ideal location of formed texture is identified with Euler angles (120°, 30-90°, 0-60°). The activated twinning planes (K_1 and K_2) are characterized as $\{10\text{-}11\}$ plane and $\{0001\}$ plane. The shear direction of $\{10\text{-}11\}$ type twinning is <10-12> axis and the twin boundaries are characterized by a misorientation of 57.42° about shear direction [25]. The orientations of the activated twinning planes are presented in the PFs of Fig. 20(a). Comparing the simulated texture variation of $\{10\text{-}11\}$ twinning mode activation with the experimental measured result in Fig. 7, it is evident that the contribution of $\{10\text{-}11\}$ twinning to the generated texture during machining of Ti-6AL-4V is very small.

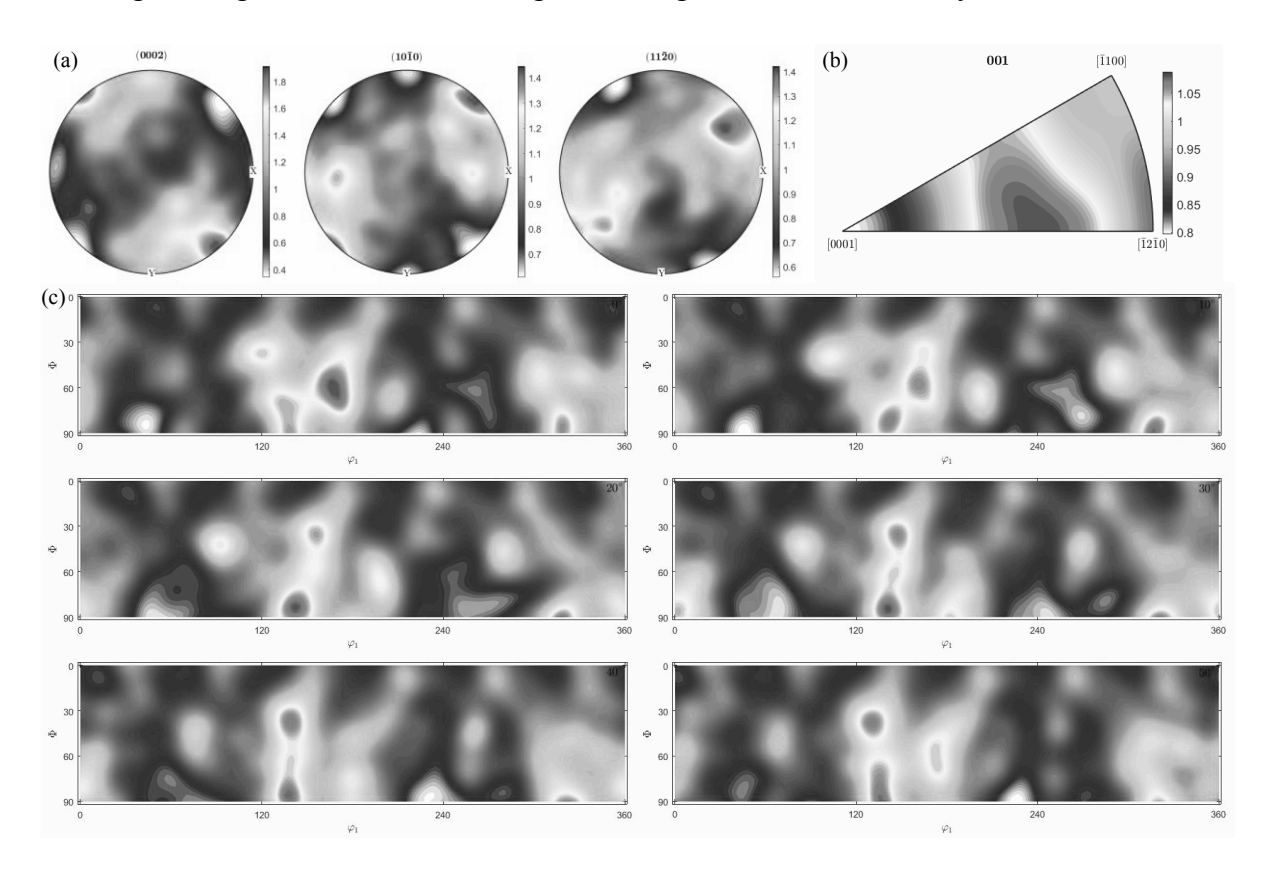


Fig. 20. Texture simulated result when only {10-11}<11-20> deformation twinning mode is activated. (a)

PFs; (b) IPF along Z direction; (c) ODF maps

4. Discussions

4.1 Slip systems activated during machining of Ti-6AL-4V

Previous studies have demonstrated that 1-st order pyramidal <c+a> slip mode is the dominant deformation mode during the deformation of magnesium [27]. However, in this work, based on the simulated results of texture evolution with the independent activities of 5 slip systems and one deformation twinning mode, it is noticeable that the effects of 1-st order pyramidal <c+a> slip mode and $\{10-11\}$ deformation twinning mode on the texture variations are not obvious. Therefore, the activities of 1-st order pyramidal <c+a> slip mode and $\{10-11\}$ deformation twinning mode are not considered in the VPSC code during the machining of Ti-6AL-4V. It is known that a <c+a> Burgers vector needs to be activated in the plastic deformation of α titanium alloys in which a minimum of five independent slip systems are required. 2-nd order pyramidal <c+a> slip mode must be activated to accommodate the reorientation trends of deformed grains during machining of Ti-6AL-4V.

For the 2-nd order pyramidal <c+a> slip family, {11-22} is the shear plane and <11-23> is the shear direction. With the cutting tool progressing, materials in the primary deformation zone undergo shear deformation. Fig. 21 shows the orientations of selected grains in the machined sub-surface of Ti-6AL-4V. A certain inclination is generated of the deformed grains with respect to the cutting speed direction. It is seen that crystal plane {11-22} is parallel to the shear plane AB and crystal direction [11-23] is parallel to the shear direction in the primary deformation zone during machining process. Under the action of shear deformation during machining process, 2-nd order pyramidal <c+a> slip mode is easily activated.

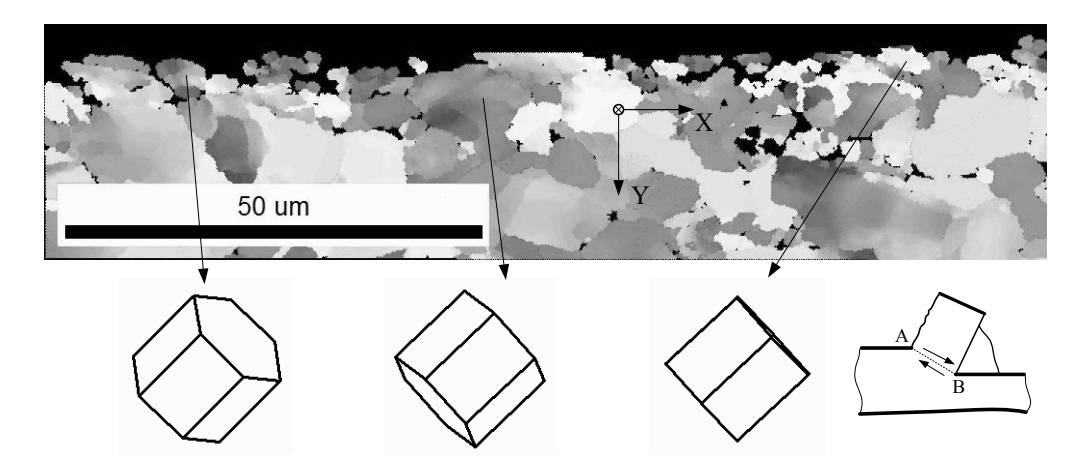


Fig. 21. Crystal orientations of selected grains in the machined sub-surface of Ti-6AL-4V created on the sample which was annealed in the bulk state at cutting speed of 550 mm/s.

Voce hardening parameters of prismatic slip, basal slip, pyramidal <a> and 2-nd order pyramidal <c+a> slip were determined by comparing the simulated results with the experimental measured results until simulated crystallographic textures matched their experimental ones. The optimized parameters are tabulated in Table 2. With considering the high cutting temperature effect, the initial CRSS values in Table 2 are different from literature [15] (Table 1). It is noted that prismatic and basal slip modes are easily activated in the initial cutting process of Ti-6AL-4V as the CRSS values of prismatic and basal slip modes are low. As the cutting tool progresses into workpiece, pyramidal <a> slip mode and 2-nd order p

Table 2 Voce hardening parameters used in this study.

Deformation mode	Prismatic	Basal	Pyramidal <a>	Pyramidal <c+a></c+a>
τ_0 (MPa)	272	290	392	454.1

τ_1 (MPa)	328	546	452	5
θ_0 (MPa)	1200	1570	1350	120

VPSC texture simulated results along deformation paths A and B based on the modified hardening parameters are presented in Figs. 22 and 23, respectively. It is noticeable that the simulated texture variations along deformation paths B and A agree well with the experimental results as shown in Figs. 7(a) - 7(d) and Figs. 11(e) - 11(h). The simulated shear texture and basal texture locations along deformation path B are close to the ideal locations specified by the Euler angles (60°, 90°, 0-60°) and ($\varphi_2+\varphi_1=30^\circ$, 0°, $\varphi_2+\varphi_1=30^\circ$). For the simulated texture variation along deformation path A, the PFs and ODF maps show that the texture locations are close to the experimental results. It is concluded that the activation of 2-nd order pyramidal <c+a> slip system is favor for the formation of C fiber shear texture. The modified Voce hardening parameters can be used to simulate the texture variation during machining of Ti-6AL-4V.

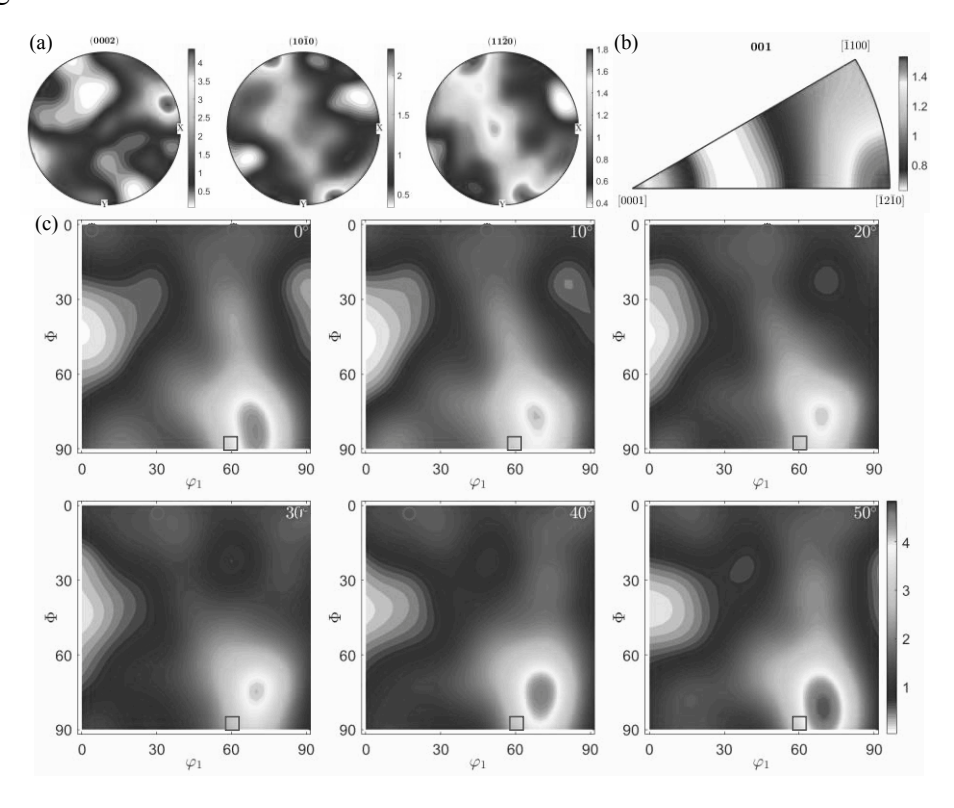


Fig. 22. VPSC simulated texture results along deformation path B created from bulk in the as-received state at cutting speed of 550 mm/s. (a) PFs; (b) IPF along Z direction; (c) ODF maps. Symbols "□" and "○" represent texture components of C fiber shear texture and basal sheet texture {0001}, respectively.

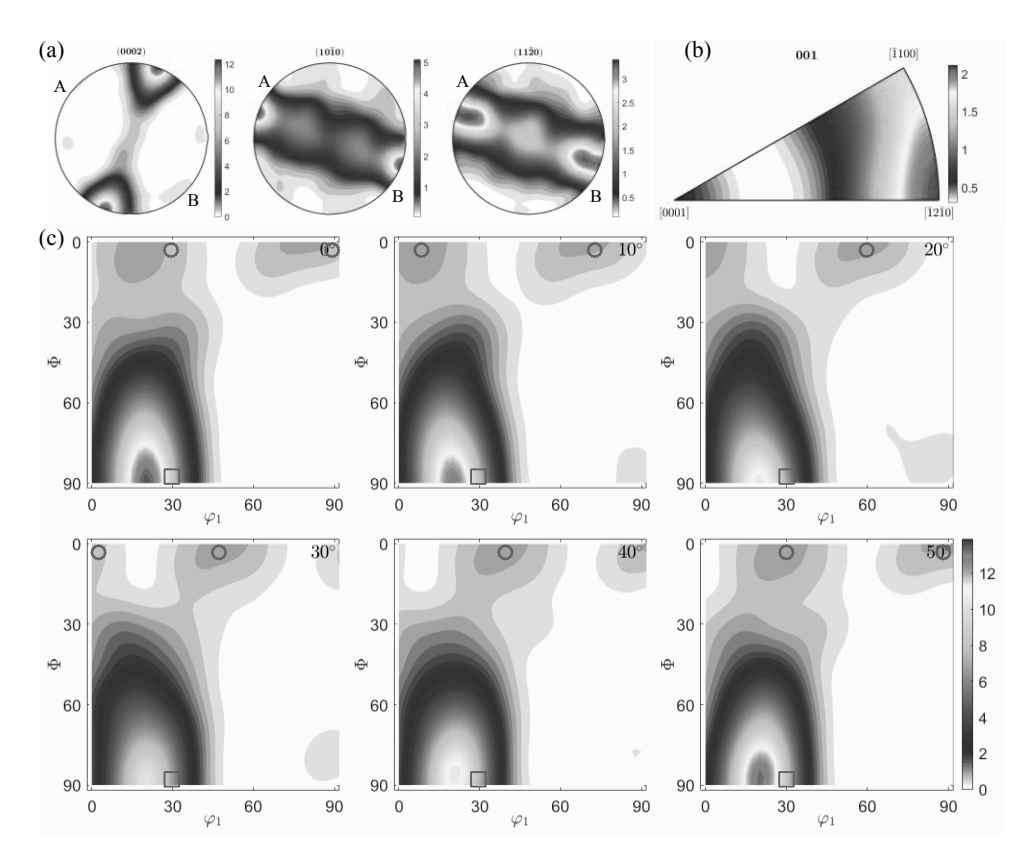


Fig. 23. VPSC simulated texture results along deformation path A created on the sample which was annealed in the bulk state at cutting speed of 1100 mm/s. (a) PFs; (b) IPF along Z direction; (c) ODF maps. Symbols "□" and "○" represent texture components of C fiber shear texture and basal sheet texture {0001}, respectively.

The relative activities of involved slip modes during machining process were obtained from the VPSC simulations. Fig. 24 plots the simulated relative activities with two calibrated sets of Voce hardening parameters. In this study, higher activities of prismatic slip, basal slip and pyramidal <a>a> slip are responsible for the texture variation in the early stage of machining. With the increase of deformation, 2-nd order pyramidal <c+a> slip becomes the

dominant deformation mode and is responsible for the generation of shear texture during machining of Ti-6AL-4V. However, as shown in Fig. 24(b), the slip mode relative activities calculated from the simulation results based on the calibrated Voce hardening parameters of literature [15] are different from the results in Fig. 24(a). In the calibrated VPSC model of literature [15], prismatic and basal slip modes are the most activated. Comparisons between these two calibrated VPSC models reveal that 2-nd order pyramidal <c+a> slip is the dominant mode for the texture evolution during machining of Ti-6AL-4V irrespective of the initial texture components.

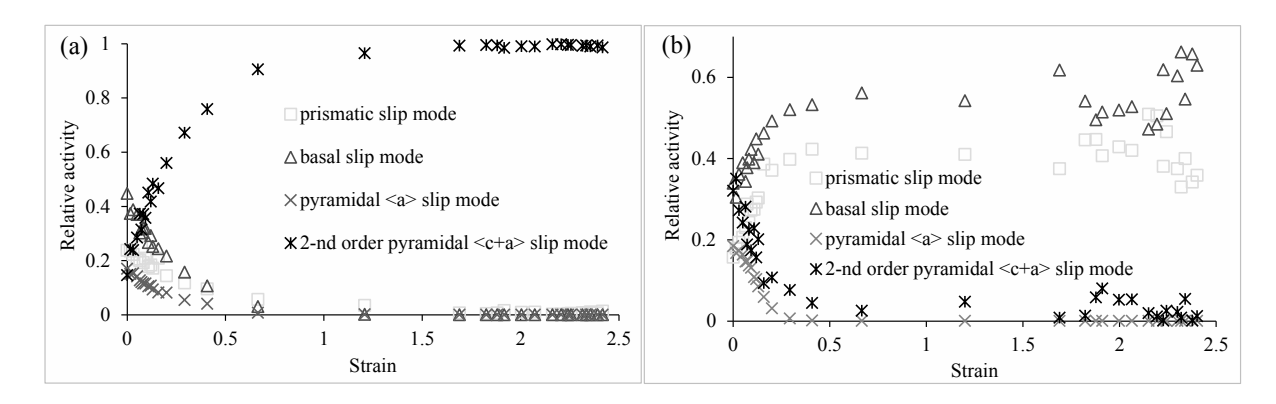


Fig. 24. Simulated relative activities of different slip modes of Ti-6AL-4V along deformation path B at cutting speed of 550 mm/s. (a) Voce hardening parameters used in this work; (b) Voce hardening parameters referenced from the research [15].

4.2 Validity of the VPSC model in simulation of mechanical property for Ti-6AL-4V

In order to demonstrate the validity of the modified VPSC model in describing the mechanical behavior of Ti-6AL-4V, a simple tension simulation in quasi-static condition is performed with comparing to the experimental result in literature [15]. A good match is observed between simulated and experimental tensile curves, as is shown in Fig. 25. It is concluded that the calibrated Voce hardening parameters in this study can accurately predict the mechanical behavior of Ti-6AL-4V.

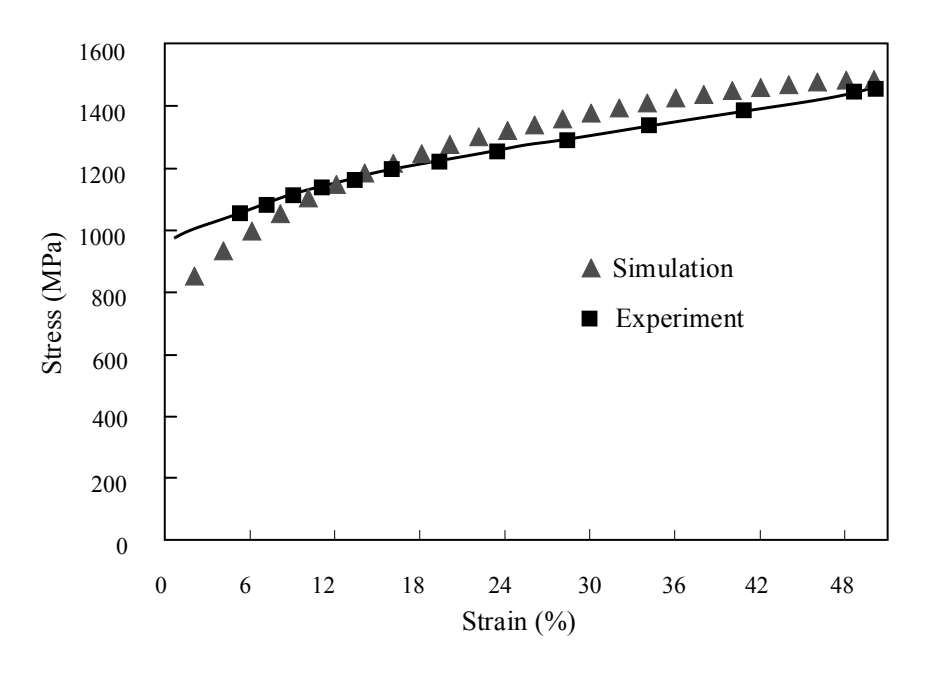


Fig. 25. Comparison of simulated and experimental tensile curves [15].

The relative activities of different slip modes are mainly depended on the deformation histories during machining of Ti-6AL-4V. As shown in Figs. 7 8, 9 and 10, the intensities of {0001} basal sheet textures along deformation path B at cutting speed of 1100 mm/s are strengthened compared with that under cutting speed of 550 mm/s. This is because the depth of machining affected zone is decreased with the increasing of cutting speed. Fig. 26 shows the variations of effective strain with distances from machined surface to bulk material at cutting speeds of 550 mm/s and 1100 mm/s. It is evident that the depth of machining affected zone at cutting speed of 550 mm/s is larger than that at cutting speed of 1100 mm/s. The extent of subsurface deformation presents gradient variation with distance from machined surface to bulk material. Correspondingly, the contribution of 2-nd order pyramidal <c+a> slip mode is decreased with distance from machined surface to bulk material. Therefore, the intensity of basal sheet texture {0001} is strengthened at cutting speed of 1100 mm/s.

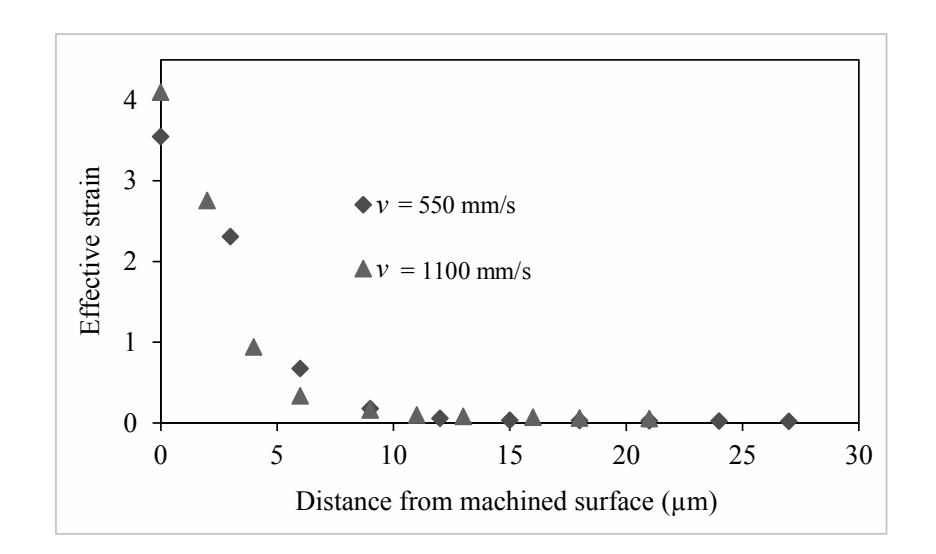


Fig. 26. Variation of strain with distance from machined surface.

A shown in Fig. 11, segmentation degree was defined to characterize the extent of deformation in two types of chips. Segmentation degrees calculated as $G_s = (h_1-h_2)/h_1$ in Figs. 11(a) and 11(e) are 0.29 ± 0.14 and 0.54 ± 0.20 , respectively. It is evident that the extent of deformation in Fig. 11(e) is larger than that in Fig. 11(a). Large deformation in Fig. 11(e) indicates that much activity of 2-nd order pyramidal <c+a> slip mode is involved during machining of Ti-6AL-4V in the as-received state. At the same cutting speed, the intensity of $\{0001\}$ basal sheet texture is strengthened in the material created from bulk in the as-received state due to the relatively low deformation.

5. Conclusions

In this study, VPSC framework and OIM characterization were used to investigate the effects of activated slip systems and deformation twinning on the texture variation during machining of Ti-6AL-4V. Simulations were performed by modifying the Voce hardening parameters in VPSC model, which allows for the activation of only one slip mode. In addition, the validity of the modified VPSC model in simulation of mechanical property of Ti-6AL-4V was verified. OIM characterization results show a same C fiber shear texture is

produced with two different initial textures of Ti-6AL-4V. VPSC simulations indicate that the combined activations of prismatic, basal, pyramidal <a> and 2-nd order pyramidal <c+a> slip modes are necessary to reproduce the experimental textures during machining of Ti-6AL-4V. Calibrated Voce hardening parameters in VPSC framework are obtained to control activities of different slip families and can predict the texture evolution satisfactorily during machining of Ti-6AL-4V. Compared results elucidate the texture evolution during machining of Ti-6AL-4V is commonly attributed to 2-nd order pyramidal <c+a> slip irrespective of material or manufacturing variables.

Acknowledgements

The authors would like to acknowledge the help of Dr. Saurabh Basu for the simulations in this work. Shankar acknowledges support from the National Science Foundation (1635966) and the Block gift program of the II VI Foundation. The work is also supported by the program of Chinese Postdoctoral Science Foundation (2019M661976) and Natural Science Foundation of Jiangsu Province for Youths.

References

- [1] M. Suresh, A. Sharma, A.M. More, R. Kalsar, A. Bisht, N. Nayan, S. Suwas, Effect of equal channel angular pressing (ECAP) on the evolution of texture, microstructure and mechanical properties in the Al-Cu-Li alloy AA2195, J. Alloy. Comp. 785 (2019) 972-983.
- [2] Z. Pu, G.L. Song, S. Yang, J.C. Outeiro, O.W. Dillon Jr, D.A. Puleo, I.S. Jawahir, Grain refined and basal textured surface produced by burnishing for improved corrosion performance of AZ31B Mg alloy, Corros. Sci. 57 (2012) 192-201.

- [3] S. Basu, Z. Wang, C. Saldana, Anomalous evolution of microstructure and crystallographic texture during indentation, Acta Mater. 105 (2016) 25-34.
- [4] O. Fergani, Z. Pan, S.Y. Liang, Z. Atmani, T. Welo, Microstructure texture prediction in machining processes, Procedia CIRP 46 (2016) 595-598.
- [5] X. Xu, J. Zhang, H. Liu, Y. He, W. Zhao, Grain refinement mechanism under high strain-rate deformation in machined surface during high speed machining Ti-6AL-4V, Mater. Sci. Eng. A 752 (2019) 167-179.
- [6] S. Basu, M.R. Shankar, Crystallographic textures resulting from severe shear deformation in machining, Metall. Mater. Trans. A 46 (2015) 801-812.
- [7] J.D. Velásquez, A. Tidu, B. Bolle, P. Chevrier, J.J. Fundenberger, Sub-surface and surface analysis of high speed machined Ti-6AL-4V alloy, Mater. Sci. Eng. A 527 (2010) 2572-2578.
- [8] N.P. Gurao, R. Kapoor, S. Suwas, Deformation behavior of commercially pure titanium at extreme strain rates, Acta Mater. 59 (2011) 3431-3446.
- [9] M. Zecevic, I.J. Beyerlein, M. Knezevic, Activity of pyramidal I and II <c+a> slip in Mg alloys as revealed by texture development, J. Mech. Phys. Solids, 111 (2018) 290-307.
- [10] A. Li, J. Pang, J. Zhao, J. Zang, F. Wang, FEM-simulation of machining induced surface plastic deformation and microstructural texture evolution of Ti-6Al-4V alloy, Int. J. Mech. Sci. 123 (2017) 214-223.
- [11] R.A. Lebensohn, C.N. Tomé, A self-consistent anisotropic approach for the simulation of plastic deformation and texture development of polycrystals: application to zirconium

- alloys, Acta Mater. 41 (1993) 2611-2624.
- [12] Q. Wang, Z. Liu, B. Wang, Q. Song, Y. Wan, Evolutions of grain size and micro-hardness during chip formation and machined surface generation for Ti-6AL-4V in high-speed machining, Int. J. Adv. Manuf. Tech. 82 (2016) 1725-1736.
- [13] http://mtex-toolbox.github.io
- [14] Q. Wang, Z. Liu, Plastic deformation induced nano-scale twins in Ti-6AL-4V machined surface with high speed machining, Mater. Sci. Eng. A 675 (2016) 271-279.
- [15] J. Galán-López, P. Verleysen, Simulation of the plastic response of Ti-6AL-4V thin sheet under different loading conditions using the viscoplastic self-consistent model, Mater. Sci. Eng. A, 712 (2018) 1-11.
- [16] N.P. Gurao, S. Sethuraman, S. Suwas, Evolution of texture and microstructure in commercially pure titanium with change in strain path during rolling, Metall. Mater. Trans. A, 44 (3) (2013), 1497-1507.
- [17] G.G. Yapici, C.N. Tomé, I.J. Beyerlein, I. Karaman, S.C. Vogel, C. Liu, Plastic flow anisotropy of pure zirconium after severe plastic deformation at room temperature, Acta Mater, 57 (16) (2009), 4855-4865.
- [18] S. Suwas, B. Beausir, L.S. Tóth, J. Fundenberger, G. Gottstein, Texture evolution in commercially pure titanium after warm equal channel angular extrusion, Acta Mater. 59 (2011) 1121-1133.
- [19] Y.N. Wang, J.C. Huang, Texture analysis in hexagonal materials, Mater. Chem. Phys. 81 (2003) 11-26.
- [20] Y. Guo, C. Saldana, W.D. Compton, S. Chandrasekar, Controlling deformation and

microstructure on machined surfaces, Acta Mater. 59 (2011) 4538-4547.

- [21] M. Knezevic, M. Zecevic, I.J. Beyerlein, J.F. Bingert, R.J. McCabe, Strain rate and temperature effects on the selection of primary and secondary slip and twinning systems in HCP Zr, Acta Mater. 88 (2015) 55-73.
- [22] A. Chapuis, Q. Liu, Simulations of texture evolution for HCP metals: Influence of the main slip systems, Comp. Mater. Sci. 97 (2015) 121-126.
- [23] B. Beausir, S. Suwas, L.S. Tóth, W.N. Kenneth, J.J. Fundenberger, Analysis of texture evolution in magnesium during equal channel angular extrusion, Acta Mater. 56 (2008) 200-214.
- [24] K.K. Gajewska, K. Sztwiertnia, J. Kawałko, K. Wierzbanowski, M. Wronski, K. Frydrych, S. Stupkiewicz, H. Petryk, Texture evolution in titanium on complex deformation paths: experiment and modeling, Mater. Sci. Eng. A, 637 (2015) 251-263.
- [25] S.F. Chen, H.W. Song, S.H. Zhang, M. Cheng, M.G. Lee, Effect of shear deformation on plasticity, recrystallization mechanism and texture evolution of Mg-3Al-1Zn alloy sheet: Experiment and coupled finite element-VPSC simulation, J. Alloy. Comp. 805 (2019) 138-152.
- [26] S. Diiorio, L. Briottet, E. Rauch, D. Guichard, Plastic deformation, damage and rupture of PM Ti-6AL-4V at 20K under monotonic loading, Acta Mater. 55 (2007) 105-118.
- [27] K. Xie, Z. Alam, A. Caffee, K.J. Hemker, Pyramidal I slip in c-axis compressed Mg single crystals, Scripta Mater. 112 (2016) 75-78.